Production and Characterization of Additively Manufactured Radiator Panels with Integral Branching Heat Pipes for High-Temperature Heat Rejection

Tatiana El Dannaoui[1], Cameron Noe[2], Dhruv Bhate[2], Christopher Greer[1], Sven Bilén[1], Bladimir Ramos Alvarado[1], William Sixel[3], Alexander Rattner[1*]

1. The Pennsylvania State University, University Park, PA, 16802
2. Arizona State University, Tempe, AZ, 85281
3. NASA Glenn Research Center, Cleveland, OH, 44135

*Corresponding Author: Alex.Rattner@psu.edu

ABSTRACT

Emerging concepts for fission surface power and nuclear electric propulsion necessitate lightweight, mechanically robust, and thermally efficient heat rejection radiators. State-of-the-art intermediate-temperature (~400 K) composite radiator assemblies have been developed based on titanium-water heat pipes bonded to metal, graphite, and carbon-fiber-based panels. NASA has identified a need for new radiator concepts that can operate at even higher temperatures (500 – 600 K), minimize thermal resistances and thermal stress failures at bond interfaces, and approach areal densities of 2 – 3 kg m^{-2}.

To meet these needs, our team is developing additively manufactured (AM) radiator panels with integral branching wicking heat pipe networks. Water is selected as the working fluid for this temperature range. Based on simulations and thermal vacuum experiments, these branching embedded heat pipe networks can efficiently distribute heat over panels for finned surface efficiencies of $\eta_f > 70\%$ at T_H = 500 K input heat.

This paper first presents laser powder-bed fusion AM strategies to produce embedded porous structures for wicking heat pipes in Inconel 718 and titanium alloys (commercially pure and Ti-6Al-4V alloys). Post-build chemical and thermal treatments are described that yield hydrophilic wicking surfaces for operation with water. Transient rate-of-rise experiments with water and acetone are reported that yield estimates for AM wick porosity (ϵ), permeability (K), and effective pore radius (r_{pore}). Based on the wick characterization results, small prototype radiator panels (75 × 125 mm) with integrated heat pipe networks were manufactured. Heat rejection performance data are presented from cold thermal vacuum testing, with heat input temperatures up to ~510 K. Future efforts will focus on improving heat pipe performance, optimizing radiator mass, and evaluating larger panels to assess scalability.

NOMENCLATURE, ACRONYMS, ABBREVIATIONS

A_c (m^2)	Cross-sectional area of the heat pipe
g (m s^{-2})	Earth's gravitational acceleration (9.81 m s^{-2})
h (m)	Water uptake height
K (m^2)	Permeability
P_{cap} (Pa)	Capillary pressure drop in the wick
P_{liq} (Pa)	Liquid pressure drop in the wick
P_{net} (Pa)	Net pressure drop in the heat pipe
P_{vap}(Pa)	Vapor pressure drop in the heat pipe
Q_{rad}(W)	Radiative heat rejected
Q_{heater}(W)	Heater power
$Q_{loss,heater}$ (W)	Radiative heat loss from the heater block
r_{pore} (m)	Pore radius
T_{avg}(K)	Radiator surface average temperature
T_H(K)	Hot temperature
T_∞ (K)	Ambient temperature of surroundings

Greek Letters:

ϵ	Porosity
ε_1	Emissivity of RUST OLEUM black paint
ε_2	Emissivity of aluminum.
η_f	Fin Efficiency
θ (degrees)	Contact angle
μ (kg m^{-1} s^{-1})	Dynamic viscosity of the fluid at ambient temperature

ρ (kg m^{-3})	Density
ρ_S (kg m^{-2})	Areal Density
σ_L (kg s^{-2})	Liquid surface tension
σ (W m^{-2} K^{-4})	Stefan Boltzmann constant ($5.67 \cdot 10^{-8}$ W m^{-2} K^{-4})

1. INTRODUCTION

Efficient and mass optimized high-temperature radiative heat rejection solutions are central to emerging fission surface power (FSP) and nuclear electric propulsion (NEP) systems. Mature spacecraft radiator technologies can operate with $T_H \sim 400$ K at mass per radiative surface area values of $\rho_S \sim 12$ kg m^{-2} (Mason, 2007), although lower ρ_S concepts have been demonstrated at prototype scale. NASA has recently proposed technical performance targets for high temperature radiators of: $T_H = 500 – 600$ K with $\rho_S = 2 – 3$ kg m^{-2} (Hyers et al., 2013; NASA TechPort, 2023).

A number of research projects have focused on development of mass efficient medium temperature heat rejection radiators ($T_H \sim 400$ K). A concept for affordable Fission Surface Power FSP) systems was investigated by NASA and the Department of Energy (DOE) for potential applications on the Moon and Mars. A candidate heat rejection system consisted of composite graphite-based radiator panels coupled with titanium-water heat pipes, operating at 400 K and having an areal density of ~3.5 kg m^{-2} (Mason et al., 2008). Large panel sections of this design were validated in thermal vacuum tests. (Tarau et al., 2016) developed and experimentally characterized a low-cost radiator for FSP applications. Each panel in their design consisted of a Ti/H_2O thermosyphon adhesively bonded to a graphite fiber-reinforced composite face sheet. The design, tested at 400 K, showed promising mass efficiency, with an areal density of ~1.5 kg m^{-2}. However, the polymer adhesive may add significant thermal resistance and limit maximum temperatures. In a complementary effort targeting $T_H = 400$ K heat rejection, Lee et al., (2020.) evaluated Ti/H_2O heat pipes with ultrasonically soldered thin aluminum radiative fin panels. Although that design was successfully able to reject the target heat output of 250 W, it reached a maximum fin efficiency of 58%. Maximum operating temperatures of such a design could be limited by the thermal expansion mismatch at the titanium to aluminum bond.

Fewer investigations have been reported for higher temperature heat rejection radiators. The SP-100 Program, a collaboration between NASA, the Department of Energy (DOE), and the Strategic Defense Initiative Organization (SDIO), began in the 1980s. The goal was to create a 2.5-MWt lithium-cooled, fast-spectrum reactor with highly enriched uranium nitride (UN) fuel pins to produce a net output of 100 kWe (Sovie, 1987). The heat rejection system concept consisted of C-C composite panels, and Zirconium alloy heat pipes (Juhasz, 2008). When operating at high temperature, the radiator faced delamination problems. Similar issues were observed in another radiator prototype composed of C-C sheets and Ti/H_2O heat pipes (Denham et al., 1994). During brazing, the composite was reported to fail by delaminating around the braze joint. It could also break off completely, leaving only a few layers bonded to the titanium.

In summary, mass efficient solutions have been demonstrated for medium temperature spacecraft heat rejection radiators. Promising concepts have also been reported for higher temperature operation. However, dissimilar material bonds between heat pipes and radiative panels have generally posed technical challenges. Polymer-based adhesives offer mechanical compliance but have limited working temperature ranges and introduce significant thermal resistance. Specialty brazes can join relevant heat pipe and radiator panel materials, but integrity challenges may occur at high temperatures due to thermal expansion coefficient (CTE) mismatch. Approaches for producing wicking structures in high temperature water heat pipes (*e.g.*, Ti/H_2O for $T_H \gtrsim 500$ K) are needed to enable operation against gravity or in micro-gravity environments.

To address the needs of FSP and NEP missions, our team is developing fully additively manufactured (AM) radiator panels with integral branched wicking heat pipe networks. Such monolithic heat pipe radiators (HPRs) can be made from high-temperature corrosion-resistant materials, avoiding the mass, thermal resistance, and integrity issues associated with material interfaces and reported in previous designs discussed earlier in this section. Water is selected as the working fluid for operation at T_H ~ 500 K. Based on initial simulations and thermal vacuum testing, these embedded branching network heat pipes may efficiently distribute heat over radiator panels, achieving finned surface efficiencies of η_f > 70% at T_H = 500 K input heat, and areal density within the desired range of ρ_S = 2-3 kg m^{-2}.

This paper first presents laser powder-bed fusion AM strategies to produce embedded porous structures for wicking heat pipes (Figure 1a-b) in Inconel 718 and titanium alloys (commercially pure and Ti-6Al-4V alloys). Note that while Inconel 718 may hydrolyze with water at high temperature (Gao et al., 2021), it is used as a test material to develop AM HPRs because of its well documented AM processing characteristics. Post-build chemical and thermal treatments are then described that yield hydrophilic wicking surfaces for operation with water. Transient rate-of-rise experiments with water and acetone are reported that yield estimates for AM wick porosity (ϵ), permeability (K), and effective pore radius (r_{pore}). Prototype small-scale radiator panels (nominally 75 × 125 mm) were designed with branching heat pipe networks, applying results from these wick characterization experiments (Figure 1c). Heat rejection performance data are presented from cold thermal vacuum testing with heat input temperatures up to T_H ~ 510 K.

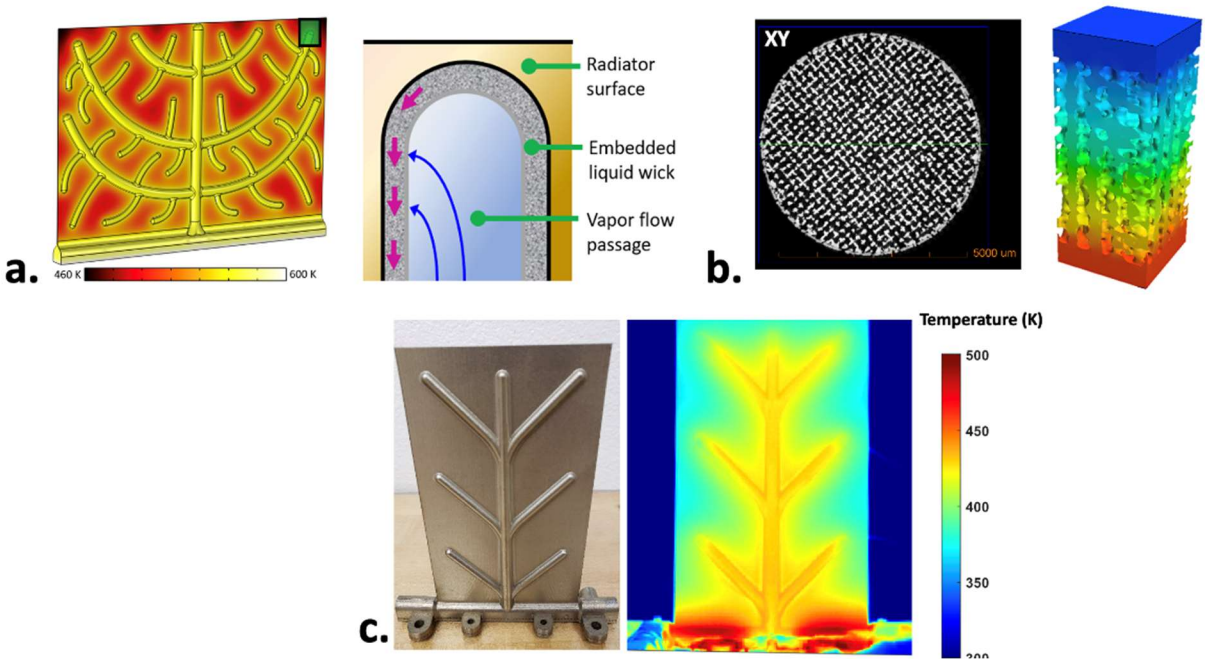

Figure 1: Scope of reported research progress. **a**. High-level illustration of the heat pipe radiator design, **b**. Additively manufactured wick development and characterization, **c**. Small-scale radiator design and manufacturing

2. ADDITIVE MANUFACTURING OF POROUS HEAT PIPE WICKS

2.1 Additive Manufacturing Strategies for Producing Inconel 718 Wicks

Three laser powder bed fusion (LPBF) fabrication strategies were explored to produce porous sections that could serve as wicks for Inconel 718 heat pipes:

a. **Structured Wicks**: Characterized by deliberate, repeating cell patterns that can potentially provide precise regulation, structural stability, and advanced features such as size gradients or local geometry modifications.
b. **Sintered Wicks**: Created by sintering the metal powder, rather than fully melting it, using low laser power build parameters. The resulting interconnected porosity between the sintered particles serves as an area for capillary driven fluid transport.
c. **Rastered Wicks**: Formed by laser scanning of the powder bed in alternating directions layer-to-layer to produce interconnected passages. Build parameters have exaggerated hatch spacing to create a square grid like network of fluid transport channels. The large hatch spacing ensures open spaces in the lasers raster pattern and prevents melt pool overlap between laser passes.

Inconel 718 wick specimens were manufactured as free-standing, vertical cylinders (6 mm diameter, 40 mm height). Specimens were produced using a GE Additive Concept Laser M2 LPBF system equipped with a 400 W peak power laser. 120 samples were made using powder feedstock that had been recycled through sieving 2 – 10 times. Layer height was set at 30 µm, and laser

power and scan speed were varied for the different specimens. After fabrication, samples were detached from the build plate, gently brushed, and cleaned with water.

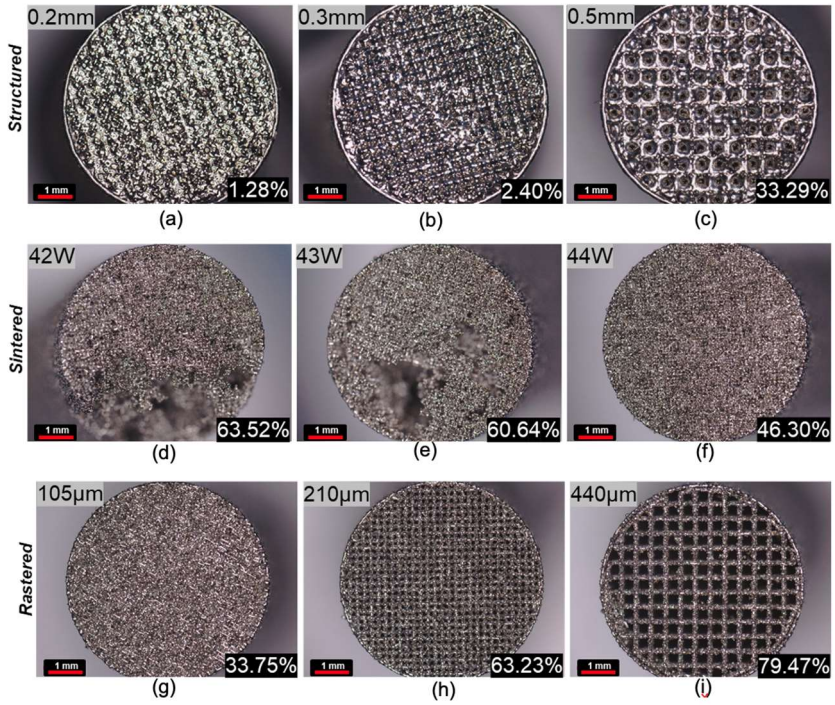

Figure 2: Example images of the different wicks fabricated using the three approaches. Wick porosity is indicated in the lower right corners. In the top left corner of all six figures: For the structured set of samples (**a**, **b**, **c**), the beam thicknesses are indicated. For the sintered set of samples (**d**, **e**, **f**), the different laser powers are mentioned. For the rastered samples (**g**, **h**, **i**), the raster line spacings are specified.

2.2 Additive Manufacturing Strategies for Titanium Wicks

Given its chemical compatibility with water (K.-L. Lee et al., 2018), low density (~4500 kg m^{-3}), and its moderate thermal conductivity (16 – 20 W m^{-1} K^{-1}), commercially pure titanium (CP-Ti) was identified as a candidate material for the AM HPR technology. In preliminary analyses of the Inconel 718 wicks, the rastered approach was found to achieve higher permeabilities, more isotropic flow properties, and fewer defects than the other processing approaches. Therefore, the CP-Ti AM wick specimens were all built with processes based on rastering. To improve permeability, specimens were also produced with raster path rotation after multiple layers rather than every other layer Figure 3. The different raster spacings and patterns, as well as laser power variations and scan speed are recorded in Table 1Table 1.

Table 1: Printing parameters and raster patterns

Raster Line Spacing (µm)	Rastering Pattern	Laser Power (W)	Laser Scan Speed (mm s^{-1})
275 and 400	Rotating every 1, 3, or 6 layers between X and Y axes	123, 147 & 184	1250

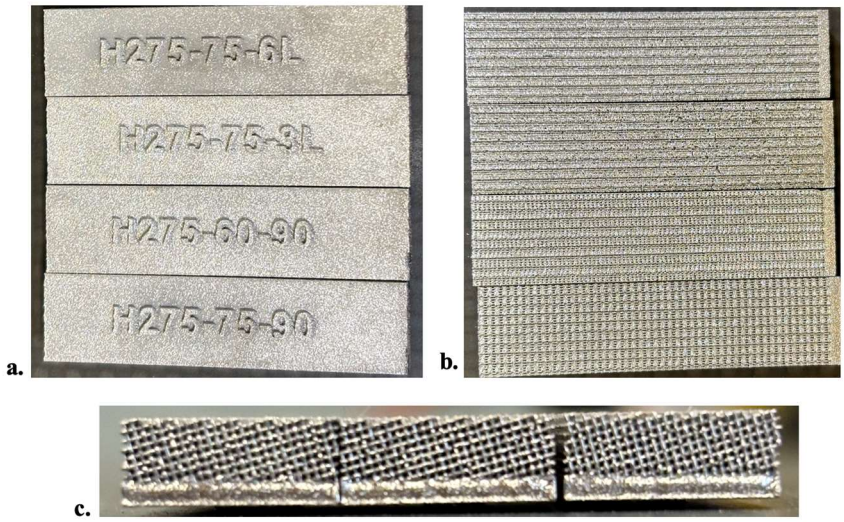

Figure 3: **a**. Labeled wick coupons post-manufacturing. For a hatch spacing of 275 µm, 75% laser power, and alternating rastering direction every 3 layers between X and Y axes, the coupon label would be "H275-75-3L", **b**. Face view of the wick sticks showing the porous surface, **c**. End view of the wick specimens showing the hatch pattern.

As AM CP-Ti builds are not performed routinely, some of the titanium specimens were produced in more commonly processed titanium alloys (Grades 5 and 23 both Ti-6Al-4V alloys). Based on guidance from the manufacturing partner, these alloys can be processed with the same LPBF settings as CP-Ti. As titanium comprises ~90% of these other alloys, it was hypothesized that they would display similar chemical and wetting properties to CP-Ti.

3. WICK TREATMENT TO IMPROVE WETTABILITY

3.1 Inconel 718 Oxidation Process to Increase Surface Wettability with Water

In the as-built state, Inconel 718 is typically poorly wetting with water, with measured room-temperature static contact angles of ~70 – 90°. Many AM specimens did not display consistent wicking with water in ambient condition tests even though they quickly saturated with other test fluids (*e.g.*, ethanol and acetone). Based on literature data, Inconel wettability with water should improve at target working conditions (~500 K) (Gojda et al., 2022), but surface modification to improve wetting could still improve wick performance. The team hypothesized that intentionally oxidizing Inconel 718 surfaces in heated air environments could evolve roughened surface features with modified chemistry that could enhance water wettability. Based

on literature data for oxidation rates of Inconel 718 (Greene & Finfrock, 2000), a test campaign was conducted in which plain specimens were heated in air at 1000°C for up to 2 hrs. Based on mass changes, the resulting oxide films were believed to be ≤ 1 μm thick. Sessile water droplet tests were performed to measure static contact angles of different specimens (Figure 4). It was found that a 40 min thermal oxidation treatment yielded nearly complete wetting, which could translate to high performing AM wicks. Longer heat treatments caused significant surface damage and are not recommended. This oxidation process was applied to all Inconel 718 wick specimens before characterization with water for rate of rise tests (see Section 4).

Figure 4: Representative images from sessile droplet static contact angle tests of water on Inconel 718 at room temperature. **a**. Droplet on untreated surface. **b**. Surface oxidized in air at 1000°C for 20 minutes. **c**. Surface oxidized in air at 1000°C for 40 minutes.

3.2 Titanium Processing to Increase Surface Wettability with Water

Titanium has been documented to rapidly passivate in most environments, leading to degraded wettability (Long et al., 2022). Limited research is available on improving hydrophilic properties of titanium specifically for heat pipes. However, titanium medical implants are widely used, and a number of strategies have been reported to increase surface activity for improved biocompatibility and cell adhesion. Some studies explored simple air-atmosphere heat treatment, such as the work of Toffoli *et al*. (2020), in which specimens were heated to 400 – 750℃. Similar to our approach for Inconel 718 specimens, this process was claimed to improve surface wettability by growing a layer of anatase TiO_2 (Kuroda et al., 2023). Other studies evaluated alkaline solution treatments with NaOH and KOH, followed by high temperature heat treatment (Kazek-Kęsik et al., 2017; Kim et al., 2013; Lim et al., 2001). These treatments may generate thin hydrophilic layers composed of sodium or potassium titanates and TiO_2 (Kazek-Kęsik et al., 2017). Previous studies evaluated chemical oxidation with hydrogen peroxide (5 – 25% concentration) followed by heat treatment at 600℃ (Khodaei et al., 2020; Khodaei & Hossein Kelishadi, 2018). It should be noted that the studies of Khodaei et al. did not report H_2O_2 concentration changes during treatments. As H_2O_2 can rapidly decompose at elevated temperatures, solution concentrations may have varied during such tests. Many studies performing chemical treatment of titanium surfaces also applied a final heat treatment step. However, the purpose of the heat treatment was not always clearly identified. (Karthega et al., 2010) argued that this thermal treatment primarily modifies the TiO_2 layer morphology to improve durability, rather than growing additional oxide.

A number of treatments were tested based on this literature to improve and preserve water wettability of the titanium wick specimens (see Table 2). Simple air-atmosphere heat treatment (1 hr at 400°C, 500°C, 550°C, 600°C) resulted in hydrophilic behavior immediately after cooling

for all specimens. However, this enhanced wettability diminished over several days in the laboratory environment. Alkaline solution treatments were applied to CP-Ti specimens at various temperatures, durations, and temperatures, followed by heat treatment at 600°C for 1 hr. These treatments resulted in very hydrophilic surfaces, but precipitates were visible in wicks, even after multiple washing cycles in an ultrasonic cleaning system. These precipitates could block flow and cause corrosion over time and would be even more difficult to remove from a long branching heat pipe network.

Chemical oxidation treatment was evaluated with 15wt% H_2O_2 solution at 60°C for 4 hours, followed by thermal treatment in air atmosphere at 600°C for 1 hour. This produced very hydrophilic CP-Ti wick specimens. The resulting hydrophilic property was found to persist for multiple months in the laboratory environment. As the residual products of the H_2O_2 reaction with titanium should only be water, oxygen and hydrogen gases, blockage of wick pores and long-term corrosion are not anticipated. Based on this performance and these considerations, the H_2O_2 treatment, followed by air-atmosphere heat treatment were adopted for subsequent development of CP-Ti HPRs.

Table 2: Evaluated treatments to improve water wettability of additively manufactured titanium wick specimens and results. Treatment described in last row (bold) was adopted for subsequent CP-Ti heat pipe radiator experiments.

Treatment	Tested Materials	Results
Heat Treatment in air atmosphere (~1 hr) at: 400, 500, 550, 600, & 750°C	CP-Ti Gr. 5 Ti Gr. 23 Ti	Increased wettability, but only temporary. Hydrophilic properties degraded within days.
NaOH chemical treatment, followed by heat treatment at 600°C	CP-Ti	Increased wettability, but large residual deposits, potentially plugging wick pores
KOH chemical treatment, followed by heat treatment at 600°C	CP-Ti	
H_2O_2 chemical treatment, followed by heat treatment at 600°C	**CP-Ti Gr. 5 Ti Gr. 23 Ti**	**Increased wettability for CP-Ti specimens, with slower degradation in wettability over time in laboratory environment.** **Gr. 5 and Gr. 23 specimens became more hydrophobic.**

4. WICK CHARACTERIZATION: POROSITY, PERMEABILITY AND PORE RADIUS ESTIMATION

4.1 Rate of Rise Experimental Set-Up and Results for AM Inconel 718 Wick Specimens.

To evaluate capillary performance of Inconel 718 wicks, dry specimens were dipped, in groups of five, into a small pool of working fluid (Deionized (DI) water, and ethanol) using a manually operated dipping rig (Figure 5a). Fluid uptake was recorded on a Nikon D3500 camera for approximately 60 seconds. Videos were examined frame by frame to identify timestamps for when

the fluid front passed the 5 mm ridges on the sample edges (Figure 5Figure 5b-c). Rate-of-rise curves were thus collected for Inconel 718 samples in both the as printed condition and after thermal oxidation. These curves Figure 5(Figure 5d) were then used to fit permeability (K) and average pore radius values (r_{pore}) with a theoretical model for capillary rise (Equation 1).

$$\frac{\rho\epsilon}{2}\frac{d^2h(t)}{dt^2} = \frac{2\,\sigma_L\,cos\theta\,\epsilon}{r_{pore}} - 2\frac{\mu}{K}h(t)\frac{dh(t)}{dt} - \rho g\epsilon h(t) \quad (1)$$

This model balances fluid inertia (left hand side) with capillary pressure (first term on right), Darcy flow resistance (second term on right), and gravitational head (last term). Contact angles (θ) are estimated as 10° for ethanol (and later acetone for CP-Ti wicks) and 15° for water for oxidized wicks.

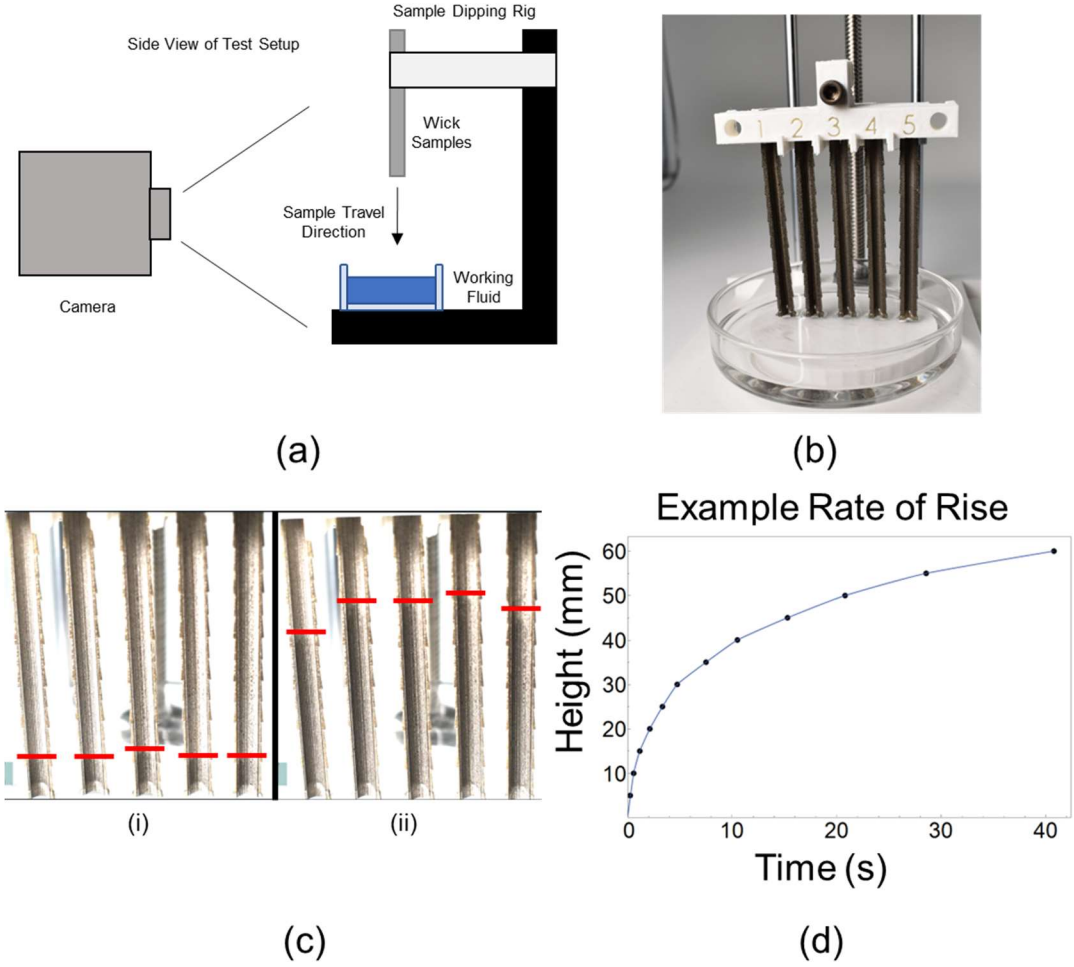

Figure 5: **(a)** Schematic of dipping rig setup, **(b)** Image of dipper setup with samples dipped into working fluid, **(c)** Images adjusted in software to better visualize the wick fluid front at two different times. Red lines indicated top of fluid front (i) Time: 3.83 s and (ii) Time: 17.88 s. **(d)** Data extracted from the video frames is compiled to create a rate of rise curve for each sample.

Example of a rate of rise curve for rastered wick sample: Wick Thickness: 0.4 mm, Print Orientation: Vertical, Working Fluid: Ethanol.

Rastered wicks with large hatch spacings (>250 µm) printed in the vertical orientation produced the greatest capillary performance ratios (K/r_{pore}). Oxidation of the Inconel wicks greatly improved the wettability of the wick surface when using water working fluid. High performing rastered wick specimens had porosity ranges of 58 – 80%, permeabilities of 100 – 440 µm^2, and average pore radius values of 42 – 168 µm (Figure 6). Some sintered wicks yielded good performance, with K/r_{pore} values slightly below the best rastered wick values. However, sintered wicks tended to have more anisotropic permeabilities.

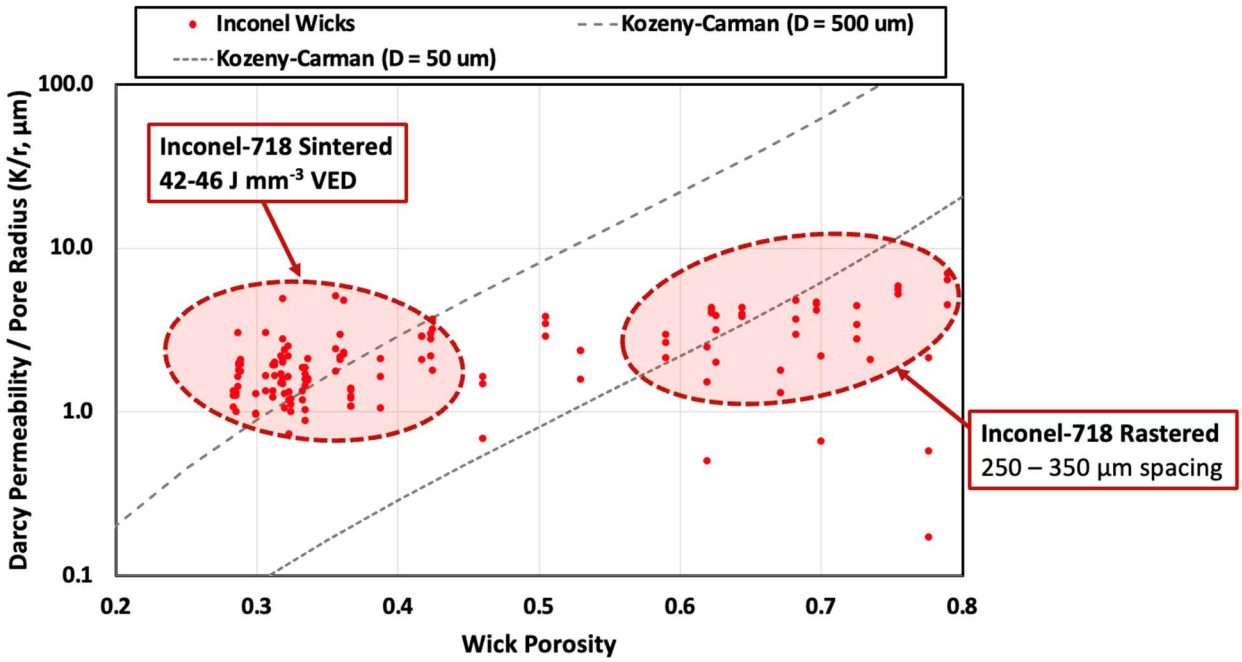

Figure 6: Darcy permeability to pore radius ratio ($\boldsymbol{K/r_{pore}}$) of oxidized Inconel 718 sintered and rastered wick specimens plotted with respect to porosity. Reported values were measured from room temperature rate-of-rise experiments with water.

4.2 Rate of Rise Experimental Set-Up and Results for AM Titanium Wick Specimens.

A transient weight-based rate-of-rise setup was prepared to estimate the effective permeabilities (K) and average pore radius values (r_{pore}) of titanium wick specimens. The specimens were rectangular shaped, having a length of 40 mm, a width of 10 mm and a thickness of 3 mm, 2 mm of which are porous. In these tests, each wick specimen was suspended from a high-sensitivity load cell over a small pool of a test liquid (acetone or deionized water, Figure 7a). Liquid was gradually added to the pool until the interface contacted the base of the wick. Transient weight measurements were collected as liquid wetted and climbed the wick specimens (Figure 7b).

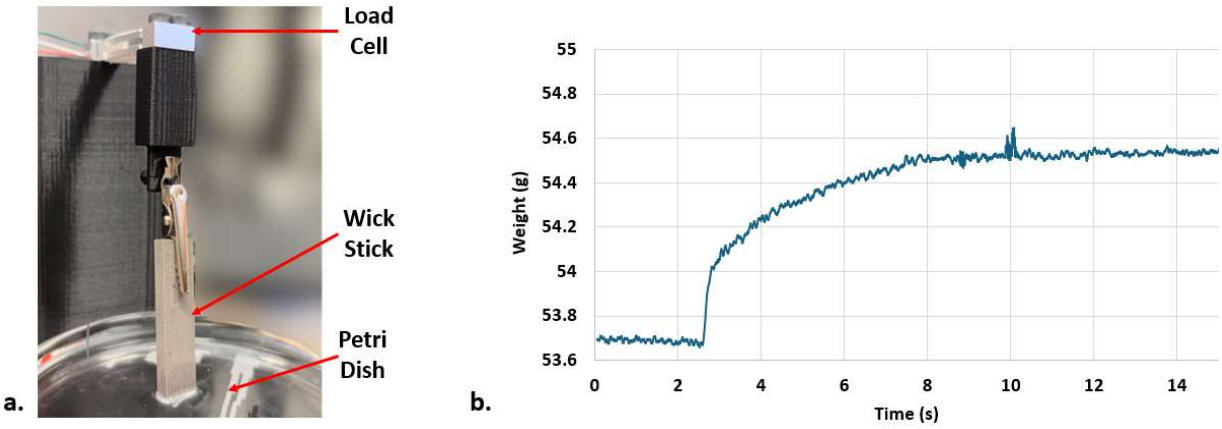

Figure 7: a. Benchtop rate-of-rise test rig, **b**. Representative load cell readings during a rate-of-rise experiment rate for a wick specimen.

Transient weight measurements were smoothed to reduce signal noise. Liquid uptake weight (mg) was converted into liquid height based on separate porosity measurements (mass-based) and assuming uniform liquid rise height through the wick cross-section. Porosity values for each wick coupon tested were obtained by first estimating the wick and solid regions volume. Using the dry mass of the coupon, along with the volumes of the wick and solid regions, the porosity for each specimen was calculated. The rate-of-rise momentum balance model (Equation 1) was then fit to measured data by minimizing integral RMS error for effective permeability (K) and average pore radius (r_{pore}). Permeability and pore radius values are summarized for titanium specimens tested using acetone and water (Table 3). Note that there is significant variability between the water and acetone measurements for K and r_{pore} for the H275-75-3L and H400-60-90 specimens obtained from this combined fitting approach. Overall performance measures (K/r_{pore}) are less affected. Additional repeatability tests are planned in the future to improve these estimates.

Table 3: Representative calculated properties of Ti wick coupons from water and acetone rate-of-rise test results. Here, contact-angle ($\boldsymbol{\theta}$) is estimated as 15° for water and 10° for acetone.

Coupon	**Porosity (ϵ)**	**Permeability (K, µm²)**	**Pore Radius (r_{pore}, µm)**	**K/r_{pore} (µm)**
H275-75-3L (Water)	34%	8970	209	43
H275-75-3L (Acetone)		3390	87	39
H275-75-6L (Water)	39%	320	36	9
H275-75-6L (Acetone)		330	24	14
H400-60-90 (Water)	56%	330	30	11
H400-60-90 (Acetone)		3550	120	30
H400-75-3L (Water)	51%	340	23	15
H400-75-3L (Acetone)		330	24	14

Darcy permeability (K) and permeability to pore radius ratio (K/r_{pore}) values for the CP-Ti wicks are summarized in Figure 8. Best performance was obtained with rastered wicks (275 – 400 µm hatch spacing) produced by rotating the rastering direction (along X- or Y-axis) every 3 build layers. These settings were adopted for full CP-Ti HPR builds. Correlation curves for properties of sintered powder wicks of comparable length scales are included for reference (Costa, 2006).

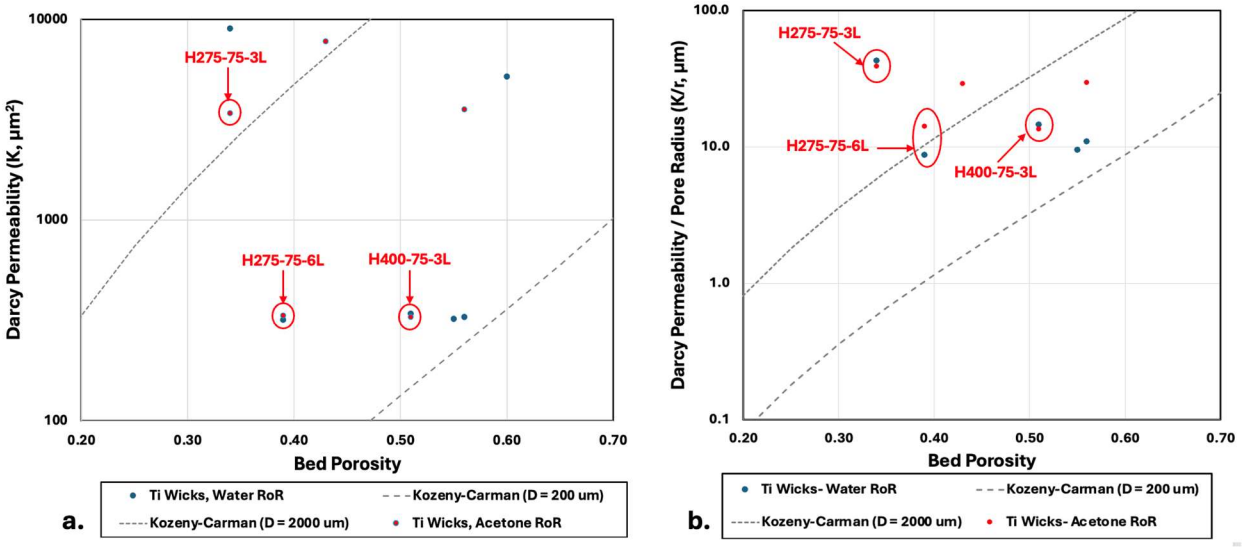

Figure 8: Measured AM titanium wick permeability (**a**) and permeability-to-pore radius ratio (**b**) compared with analytic model values for packed beds of spheres of comparable length scales. The wicks with the most consistent results are highlighted and labeled in red.

5. HEAT PIPE RADIATOR DESIGN, PRODUCTION, AND TESTING

5.1 Design of Prototype Heat Pipe Radiator Specimens

Prototype AM Ti radiator panels with integral branching heat pipes were produced with high performing internal rastered wick structures described in Sections 2-4. The main panel sections of the radiators were 75 × 125 mm with a fin web section thickness of 500 µm (Figure 9a-b). Four mounting tabs on the base are used to attach an external heater unit. Two outer tabs are used to suspend the HPR and heater assembly on thin threaded rods to minimize conduction losses during thermal vacuum testing. A compact manifold assembly in the base allows charging of working fluid, vacuum of non-condensable gases, and sealing during testing.

The HPR specimens have a horizontal evaporator section on the base, which connects to a vertical central trunk that branches into 6 angled sections. A double-pipe geometry is employed in the horizontal evaporator to increase heat transfer area and reduce the risk of critical heat flux or boiling-limited dry-out (

Figure 9a-b). The overall layout and spacing of branches were selected to achieve radiative fin surface efficiency of $\eta_f \sim 75\%$ assuming isothermal heat pipes at ~500 K. Based on the findings

discussed in Section 4, the best working wicking parameters were implemented in the small-scale CP-Ti radiator sheets and summarized in Table 4.

Table 4: Summary of prototype small-scale heat-pipe radiator dimensions and wick parameters.

Parameters	**Values**
Total Height of the design (mm)	131.20
Total Width of the design (mm)	109.53
Height of the radiator fin (mm)	125
Width of the radiator fin (mm)	75
Fin Thickness (μm)	500
Wick Thickness Range (mm)	0.49 (thin branches) – 0.95 (centerline branch)
Vapor Diameter Range (mm)	1.50 (thin branches) – 4.64 (centerline branch)
Theoretical Panel Mass (g)	87.5
Wick Raster Line Spacing (μm)	275 and 400
Raster Strategy	Alternating printing directions between X and Y axes every 3 or 6 layers

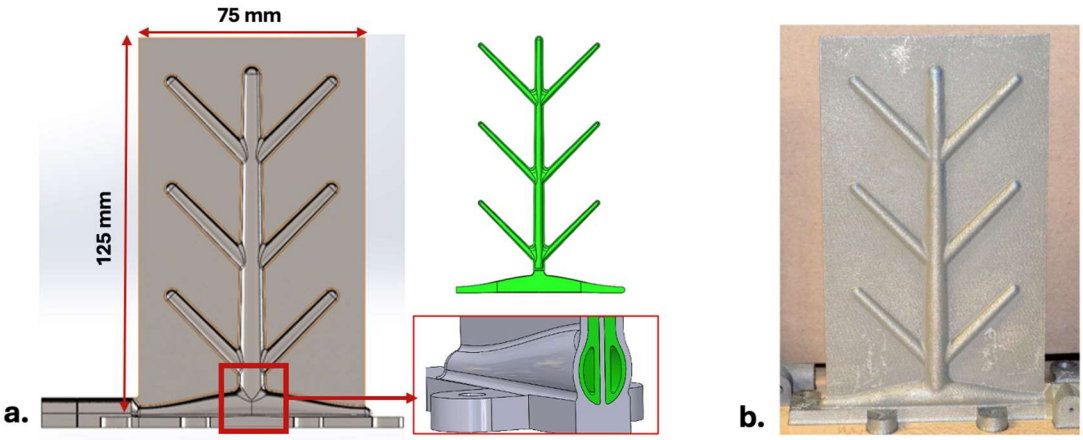

Figure 9: a. CAD drawing of the radiator panel, the wick in green and a cross-sectional view of the evaporator region, b. Produced radiator panel.

Multiphysics simulations were conducted to guide this design accounting for solid domain conduction, vapor flow in the internal passages, porous media transport in the wick (with experimentally measured permeability and pore radius values), liquid-vapor phase change at the wick interface, and external radiation (Figure 10). Vapor flow and wick cross-sections were adjusted based on simulations for this design so that the total predicted pressure range in the heat pipe network: $\Delta P_{net} = \Delta P_{wick} + \Delta P_{vapor} \sim 200$ Pa. This is safely below the expected capillary pumping capacity of $\Delta P_{cap} = 2\sigma/r_{pore} \sim 630$ Pa at temperature and should therefore avoid local wick dry out. The employed permeability (K = 2000 μm^2) and a pore radius (r_{pore} = 100 μm) values were representative of measurements described in Section 4.2.

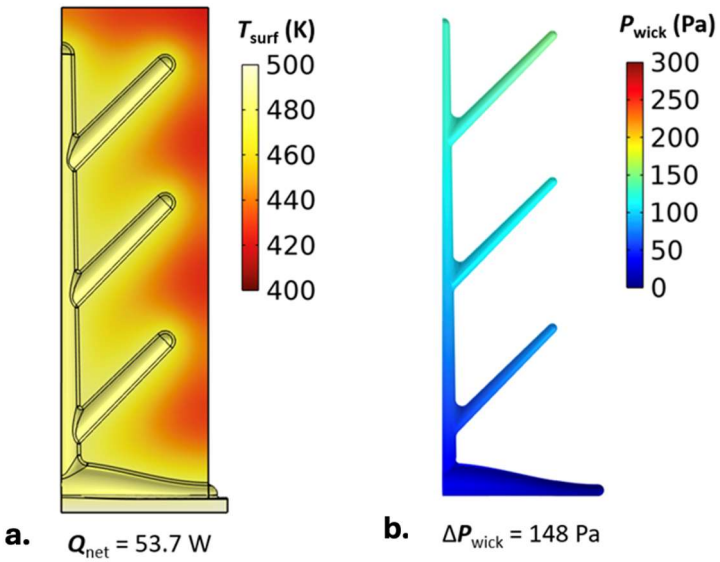

Figure 10: Representative simulation predictions for: **a**. External surface temperature and **b**. Wick pressure drop for CP-Ti radiator (quarter symmetry section).

5.2 Post-Build Processing of Radiator Prototypes

After LPBF manufacturing, the HPR specimens were mechanically de-powdered. A cyclic batch chemical treatment system was built to apply the H_2O_2 solution treatment to the interior of the branching heat pipes network. So far, one specimen has been processed, which has a wick raster line spacing of 275 μm with scan direction rotating every 3 layers. In this process, 15% H_2O_2 solution was forced into the heat pipes with ~600 kPa absolute air-overpressure for 2-minute intervals. A check valve on the solution reservoir allowed continuous venting of gas to prevent H_2 and O_2 buildup from the hydrolysis and H_2O_2 decomposition reactions. Then, vacuum would be applied (to ~10 kPa absolute) for ~10 s to remove evolved gases from the heat pipe network. This approach was developed to ensure that solution reaches the full internal heat pipe network, and that gas build-up does not displace liquid solution, and prevent local oxidation (Figure 11a). During treatment, the HPR specimen (Figure 11b) was submerged in a heated water bath to maintain temperature at ~60°C. After solution treatment, the radiator was flushed with deionized water and heat treated at 600°C in an air atmosphere furnace for one hour.

Finish machining operations (porting, lapping heated based) were then performed. The radiator was media blasted to remove scale and painted flat black with a high-emissivity spray paint (RUST-OLEUM specialty high heat; ε ~ 91-94% (Bellamy et al., 2023)). The paint was thermally cured per the manufacturer specification.

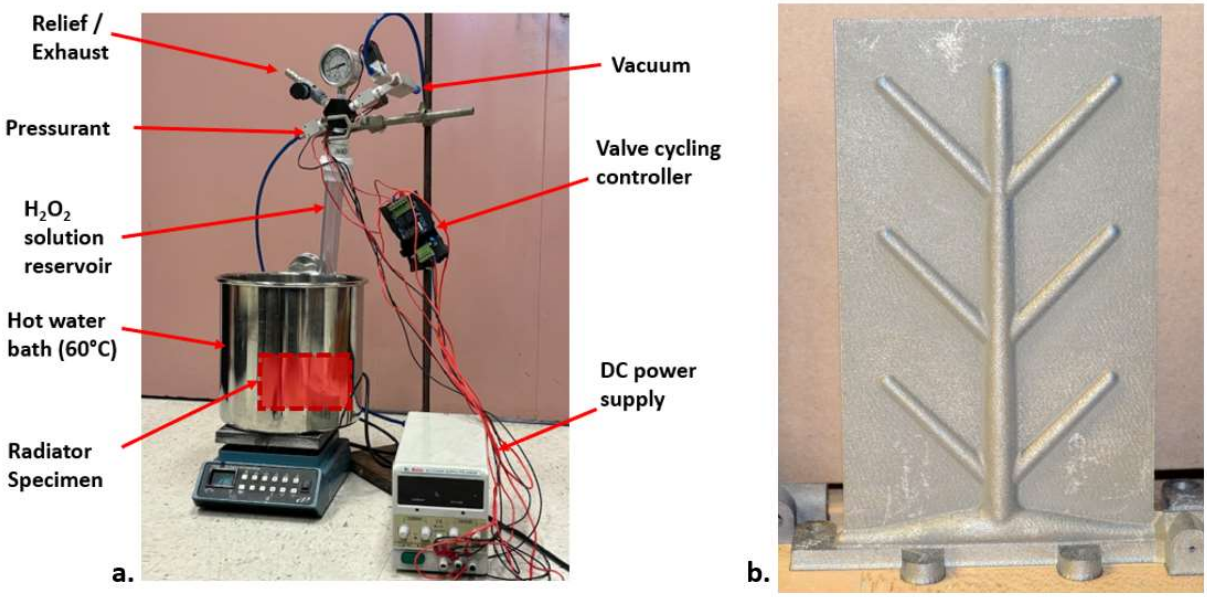

Figure 11: **a**. Annotated picture of set-up for the hydrogen peroxide oxidation treatment, **b**. Picture of an untreated CP-Ti small-scale radiator.

5.3 Thermal Characterization Test Facility and Procedure

A copper heater block was mounted to the radiator base with thermal contact facilitated by a specialty high-temperature vacuum-rated thermal compound (silver-loaded Aremco Heat-Away 641-EV). The copper heater was loosely wrapped with a couple layers of aluminum foil to limit radiative heat loss. The HPR and heater assembly were mounted on two long 4 mm diameter threaded rods to limit conductive heat loss (Figure 12).

The HPR was installed horizontally (large faces approximately parallel to ground) in a liquid-nitrogen (LN2) cooled sub-enclosure inside a vacuum chamber (Figure 13). This approximates neutral-gravity operation in a cold space environment. The inside of the sub-enclosure enclosure was coated with Aeroglaze Z306, a high-vacuum-rated paint with a high emissivity of approximately 0.95 (McCroskey et al., 2000).

The copper heater block was regulated at specified temperatures with a proportional output PID process controller (Dwyer Love Controller 16B). An AC power transducer (CR Magnetics CR6210-150-1) was used to measure instantaneous heater power ($\pm$1 W uncertainty). A LabJack T7 data acquisition unit was employed to collect thermocouple and heater power measurements.

Sealed thermocouple feedthroughs were used to measure surface temperatures on 9 points around the LN2 cooled sub-enclosure, the copper heater block, and two points on the underside of the HPR specimen. A vacuum-compatible, miniature long-wave infrared thermal imaging camera (FLIR Boson 320 60Hz) thermal imaging camera was used to measure surface temperature distributions on the top face of the radiator (Figure 14).

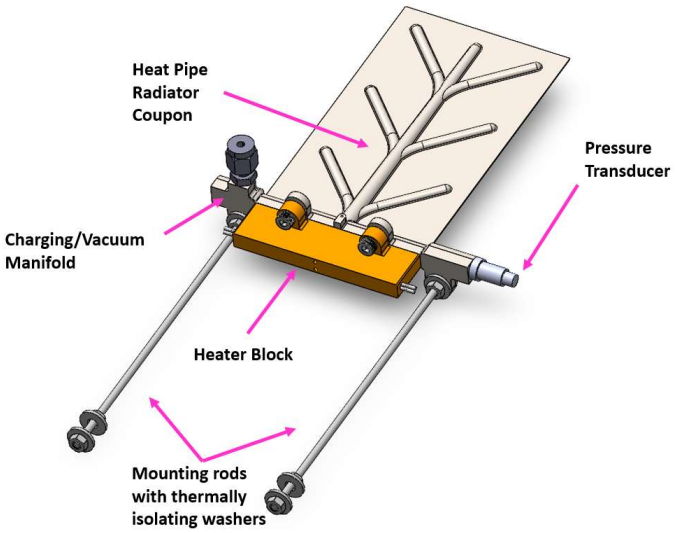

401

402 **Figure 12**: Rendering of HPR assembly for thermal vacuum testing. Note, the final CP-Ti design
403 did not include a pressure transducer port.

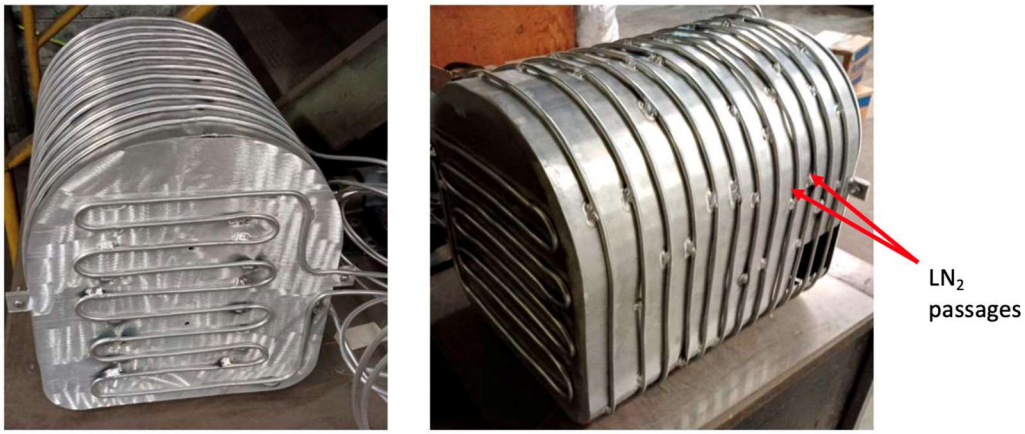

404

405 **Figure 13**: Aluminum sub-enclosure featuring the cooling LN_2 tubing. Note that the final installed
406 unit has nearly continuous solder applied along cooling tube lines.

407 The test platform was installed in the vacuum chamber and verified for proper operation with
408 cryogenic coolant supply. This facility was successfully employed to perform a set of vacuum
409 characterization studies for the HPR specimens with heat inputs up to 508 K (235°C). The chamber
410 reached a vacuum pressure of 10^{-5} torr (~$1.3 \cdot 10^{-3}$ Pa).

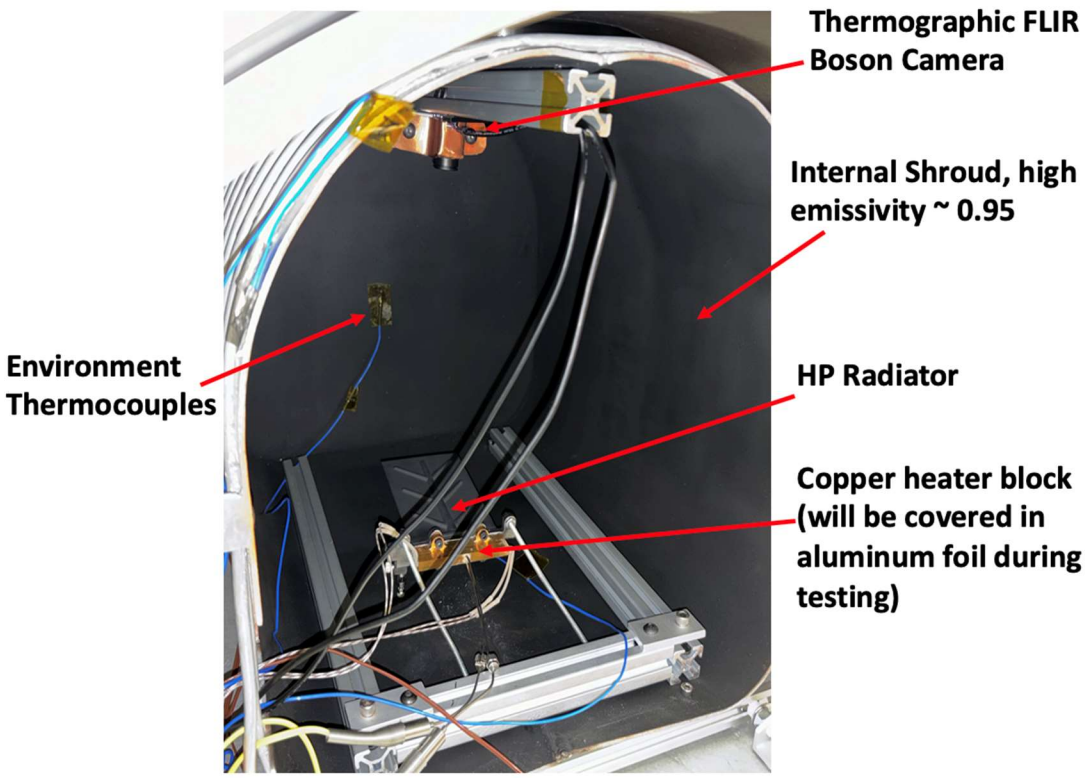

Figure 14: Labeled diagram of heat pipe radiator test facility, featuring the shroud, heater block assembly and the thermographic camera installed in the thermal vacuum chamber.

To charge the radiator, deionized water was injected into the heat pipe network using a syringe equipped with a fine-gauge needle. The radiator was heated to a moderate temperature (~50°C). Vacuum was then cyclically applied to the radiator through a valve to remove non-condensable gases and reduce the liquid charge to an appropriate level. After each vacuum cycle, the radiator was inspected with thermal imaging to determine whether non-condensable gases had been removed (corresponding to large temperature variations in the evaporator) and whether excess fluid charge was present (corresponding to flooded, non-isothermal heat pipe branch tips). This sequence was repeated until the entire heat pipe network was fully activated and exhibited an isothermal condition.

5.4 Thermal Characterization Results for Titanium Heat Pipe Radiator

Thermal imaging results are presented for the radiator test in Figure 16 for heater block temperatures of T_H = 373, 423, 473, and 508 K. Overall, the thermal imaging results showed successful operation of the heat pipe network without evaporator dry out.

In earlier stages of the project, the team investigated Inconel 718 radiator panels produced with different printing strategies. Thermal vacuum testing of those coupons showed significant dry-out of the evaporator at working temperature. This can be a result of low permeability or defects in the wick structure. It may also be that water charge was not optimal during the tests (Figure 15).

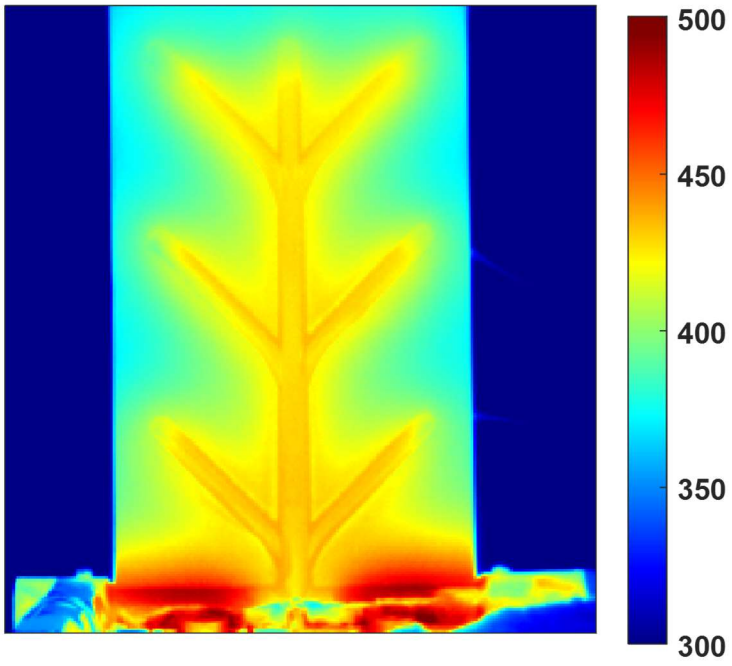

Figure 15: Vacuum testing thermal imaging results for previously investigated Inconel 718 radiator panel. Condenser portion of the heat pipe network is relatively isothermal, but there is significant dryout in the lower evaporator.

In thermal images featured in Figure 16b-d, the cryogenically cooled background temperature is reported as uniform at 119.9 K. This is slightly below the average surface thermocouple temperature measurements of 139 – 145 K. It is suspected that the thermal imaging camera firmware applies thresholding to such cryogenic temperature readings, but the manufacturer has not responded to requests for documentation.

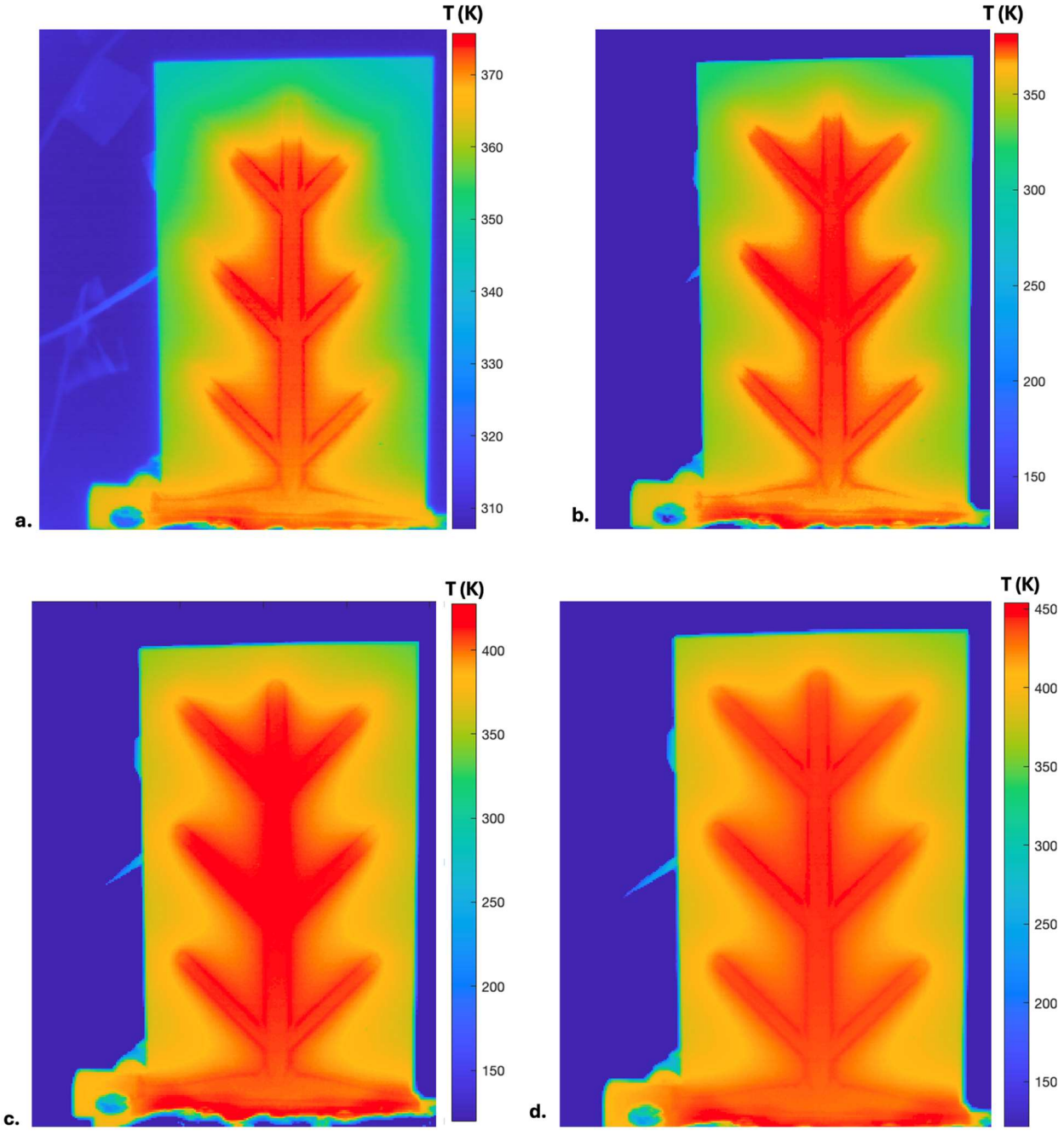

Figure 16: Thermal vacuum testing thermal images for titanium radiator prototype at: **a**. T_H = 100°C (373.15 K), **b**. 150°C (423.15 K), **c**. 200°C (473.15 K), **d**. 235°C (508.15 K).

It was observed that the HPR performance at different temperatures was sensitive to fluid charge. Due to the nature of the charging process, the exact fluid quantity in the radiator was not quantitively measured. A slightly greater liquid charge was needed to fully activate all heat pipe branches at high temperatures/heat input rates (Figure 16c-d). However, this same charge resulted

in degraded performance at lower heating rates (Figure 17a-b), with outer tips of heat pipe branches registering lower temperatures. We believe that excess liquid "floods" those heat pipe tips at lower heat input rates, rather than continuously circulating along the wick, as reported in previous similar cases (D. H. Lee & Bang, 2023). Reduced wick charge can fully activate heat pipe networks at lower temperatures but was found to cause high-temperature evaporator dry-out (Figure 17).

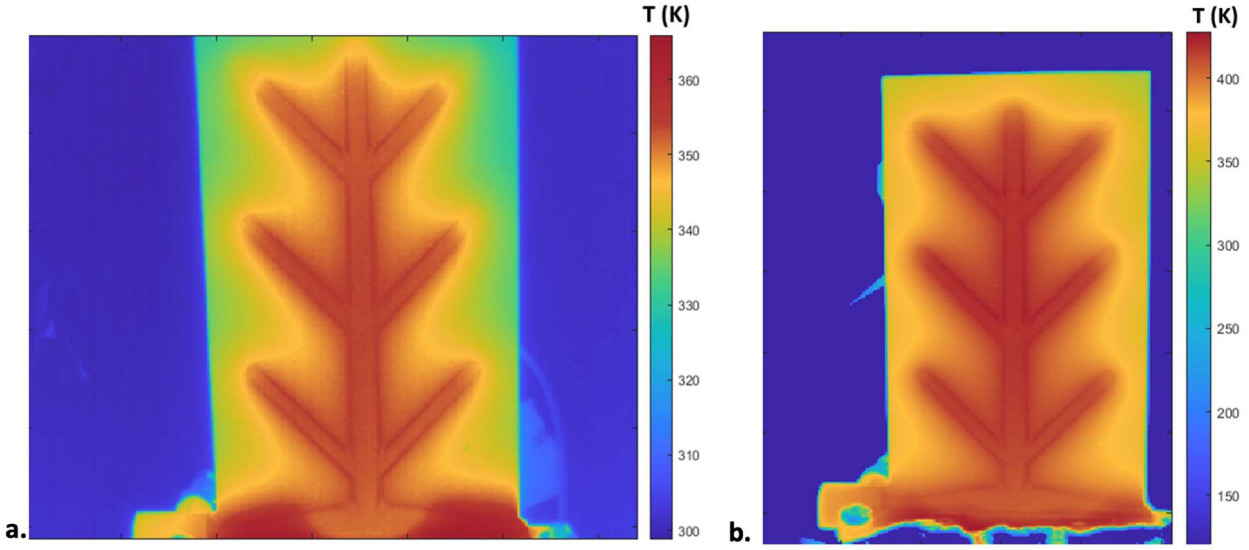

Figure 17: **a**. Temperature distribution at $\boldsymbol{T_H}$ = 200°C, charge optimized for $\boldsymbol{T_H}$ = 50°C, dry out at the evaporator, **b**. Temperature distribution at $\boldsymbol{T_H}$ = 200°C, charge optimized for $\boldsymbol{T_H}$ = 150°C, no dry out observed at the evaporator.

Overall radiator performance can be quantified by modeling the HPR as a gray diffuse emitter in a large isothermal environment (Equation 2). Here, Q_{heate} is the measured heater block input power ($\pm$1 W), $Q_{loss,heater}$ is the radiated heat lost from the copper heater block and was estimated by running the heater in vacuum at the same temperature ranges as the radiator tests. ε_1 is the high temperature paint emissivity (0.94 $\pm$0.02) (García-Baños et al., 2022). σ is the Stefan-Boltzmann constant. A_s is the surface area of the radiator with an uncertainty of 5% (186 ± 14 cm^2) due to the slight differences in dimensions between the actual CAD drawing and manufactured prototype. T_{avg} is the effective average HPR surface temperature (solved implicitly). At each operating temperature, T_∞ is an average of the values collected from 9 thermocouples distributed on the inside of the LN2 cooled sub-enclosure over the span of 5 minutes after stabilization. The heater power was averaged in a similar manner over the same time interval. Results are summarized in Table 5.

$$Q_{rad} = q''_{rad} A_s = Q_{heater} - Q_{loss,heater} = \varepsilon_1 \, \sigma \, A_s (T_{avg}^4 - T_\infty^4) \quad (2)$$

$$Q_{loss,heater} = \varepsilon_2 \, \sigma \, A_{S,copper\ block} \, (T_H^4 - T_\infty^4) \quad (3)$$

$$\eta_f = Q_{rad}/\varepsilon_1 \sigma (T_H^4 - T_\infty^4) \quad (4)$$

Table 5: Summary of heat transfer measurements and results from thermal testing of prototype titanium heat pipe radiator.

T_H (K)	Q_{rad} (W)	q''_{rad} (W m^{-2})	$Q_{loss,heater}$ (W)	T_∞ (K)	T_{avg} (K)	η_f (%)
376 ± 1	16.5 ± 1.1	880 ± 70	1.4 ± 0.5	145 ± 5	361 ± 8	85 ± 7
425 ± 1	25.9 ± 1.3	1380 ± 100	2.3 ± 0.8	139 ± 5	403 ± 7	80 ± 6
475 ± 1	35.2 ± 1.6	1880 ± 130	3.6 ± 1.3	140 ± 5	434 ± 8	70 ± 5
510 ± 1	44.9 ± 2.0	2390 ± 160	4.8 ± 1.7	140 ± 5	461 ± 8	67 ± 5

Overall, these results indicate consistent performance of the HPR prototypes over a range of heat input temperatures up to 510 K. Fin efficiency does degrade with increasing temperature, which is consistent with conduction theory for radiating fins. However, overall surface efficiency maintained in the target range of $\eta_f \gtrsim 70\%$ for the tested conditions.

6. CONCLUSIONS

This study details progress toward development of monolithic additively manufactured high temperature heat-pipe radiators (HPRs) with integral branching wicking heat pipes. Manufacturing strategies were developed to produce porous wicking structures in Inconel 718 and titanium alloys using laser powder bed fusion. Post-processing steps were developed to modify additively manufactured wick surfaces to be hydrophilic. Experiments were conducted to measure capillary properties of wicks, including permeability (K), porosity (ϵ), and average pore radius (r_{pore}). These tests identified wick fabrication strategies that yield high performance metrics (K and K/r_{pore}), compared with conventionally manufactured wicks. These wick parameters and post-processing steps were applied to produce full CP-Ti HPR prototypes. A prototype HPR was tested in a relevant cryogenic thermal environment. With the appropriate fluid charge, the specimen achieved nearly isothermal heat pipe operation and $\eta_f \gtrsim 67\%$ for heat input at T_H up to 510 K with an areal density of ~ 2.13 kg m^{-2}. This aligns with objectives proposed by NASA.

In upcoming work, the team is planning to evaluate the AM branching HPR concept for larger prototypes to assess scalability. Modeling studies are underway to optimize layout and geometry of branching heat pipe networks for larger HPRs. Further work is planned to integrate coupling fluid loop heat transfer in evaporator sections and assess practical factors, such as micrometeoroid and orbital debris impact risks and deployment strategies for large HPR arrays.

ACKNOWLEDGMENTS

The authors wish to acknowledge generous support from the U.S. National Aeronautics and Space Agency Space Technology Mission Directorate – Early Stage Innovations (Grant 80NSSC22K0260).

REFERENCES

Bellamy, G. T., DiDomizio, M. J., Patel, M. K., & McKinnon, M. B. (2023). Characterization of high-temperature paints for infrared thermography in fire research. *Fire Safety Journal*, *137*, 103775. https://doi.org/10.1016/j.firesaf.2023.103775

Costa, A. (2006). Permeability-porosity relationship: A reexamination of the Kozeny-Carman equation based on a fractal pore-space geometry assumption. *Geophysical Research Letters*, *33*(2), 2005GL025134. https://doi.org/10.1029/2005GL025134

Denham, H. B., Koester, J. K., Clarke, W., Juhasz, A. J., El-Genk, M. S., & Hoover, M. D. (1994). NASA Advanced Radiator C[Single Bond]C Fin Development. *AIP Conference Proceedings*, 1119–1127. https://doi.org/10.1063/1.2950112

Gao, Z., Ji, F., Cheng, D., Yin, C., Niu, J., & Brnic, J. (2021). Hydrolysis-Based Hydrogen Generation Investigation of Aluminum System Adding Low-Melting Metals. *Energies*, *14*(5), 1433. https://doi.org/10.3390/en14051433

García-Baños, B., Chiariotti, P., Napolitano, R., Pandarese, G., Navarrete, L., Marco Revel, G., & Catalá-Civera, J. M. (2022). Dielectric and optical evaluation of high-emissivity coatings for temperature measurements in microwave applications. *Measurement*, *198*, 111363. https://doi.org/10.1016/j.measurement.2022.111363

Gojda, F., Loulakis, M., Papoutsakis, L., Tzortzakis, S., Chrissopoulou, K., & Anastasiadis, S. H. (2022). Altering the Surface Properties of Metal Alloys Utilizing Facile and Ecological Methods. *Langmuir*, *38*(16), 4826–4838. https://doi.org/10.1021/acs.langmuir.1c03431

Greene, G. A., & Finfrock, C. C. (2000). *Oxidation of Inconel 718 in air at temperatures from 973 K to 1620 K* (BNL-52620). Brookhaven National Lab.

Hyers, R. W., Tomboulian, B. N., Craven, P., & Rogers, J. (2013). Lightweight, High-Temperature Radiator for Space Propulsion. *Industrial Engineering*.

Juhasz, A. (2008, July 28). High Conductivity Carbon-Carbon Heat Pipes for Light Weight Space Power System Radiators. *6th International Energy Conversion Engineering Conference (IECEC)*. 6th International Energy Conversion Engineering Conference (IECEC), Cleveland, Ohio. https://doi.org/10.2514/6.2008-5784

Karthega, M., Nagarajan, S., & Rajendran, N. (2010). In vitro studies of hydrogen peroxide treated titanium for biomedical applications. *Electrochimica Acta*, *55*(6), 2201–2209. https://doi.org/10.1016/j.electacta.2009.11.057

Kazek-Kęsik, A., Leśniak, K., Zhidkov, I., Korotin, D., Kukharenko, A., Cholakh, S., Kalemba-Rec, I., Suchanek, K., Kurmaev, E., & Simka, W. (2017). Influence of Alkali Treatment on Anodized Titanium Alloys in Wollastonite Suspension. *Metals*, *7*(9), 322. https://doi.org/10.3390/met7090322

Khodaei, M., & Hossein Kelishadi, S. (2018). The effect of different oxidizing ions on hydrogen peroxide treatment of titanium dental implant. *Surface and Coatings Technology*, *353*, 158–162. https://doi.org/10.1016/j.surfcoat.2018.08.037

Khodaei, M., Nejatidanesh, F., Shirani, M. J., Iyengar, S., Sina, H., Valanezhad, A., & Savabi, O. (2020). Optimum temperature and chlorine ion concentration for hydrogen peroxide treatment of titanium dental implant material. *Journal of Materials Research and Technology*, *9*(6), 13312–13319. https://doi.org/10.1016/j.jmrt.2020.09.040

549 Kim, C., Kendall, M. R., Miller, M. A., Long, C. L., Larson, P. R., Humphrey, M. B., Madden,
550 A. S., & Tas, A. C. (2013). Comparison of titanium soaked in 5M NaOH or 5M KOH
551 solutions. *Materials Science and Engineering: C*, *33*(1), 327–339.
552 https://doi.org/10.1016/j.msec.2012.08.047
553 Kuroda, P. A. B., De Mattos, F. N., Grandini, C. R., & Afonso, C. R. M. (2023). Effect of heat
554 treatment on the phases, pore size, roughness, wettability, hardness, adhesion, and wear
555 of Ti-25Ta MAO coatings for use as biomaterials. *Journal of Materials Science*, *58*(39),
556 15485–15498. https://doi.org/10.1007/s10853-023-08979-2
557 Lee, D. H., & Bang, I. C. (2023). Experimental investigation of thermal behavior of overfilled
558 sodium heat pipe. *International Journal of Heat and Mass Transfer*, *215*, 124449.
559 https://doi.org/10.1016/j.ijheatmasstransfer.2023.124449
560 Lee, Kuan-Lin & Tarau, Calin & Anderson, William & Beard, Derek. (2020). Titanium-Water
561 Heat Pipe Radiators for Space Fission Power System Thermal Management.
562 Microgravity - Science and Technology. 32. 10.1007/s12217-020-09780-5.
563 Lee, K.-L., Anderson, W. G., & Tarau, C. (2018, July 9). Titanium-Water Heat Pipe Radiators
564 for Kilopower System Cooling Applications. *2018 International Energy Conversion*
565 *Engineering Conference*. 2018 International Energy Conversion Engineering Conference,
566 Cincinnati, Ohio. https://doi.org/10.2514/6.2018-4581
567 Lim, Y. J., Oshida, Y., Andres, C. J., & Barco, M. T. (2001). *Surface Characterizations of*
568 *Variously Treated Titanium Materials*.
569 Long, J., Li, Y., Ouyang, Z., Xi, M., Wu, J., Lin, J., & Xie, X. (2022). A universal approach to
570 recover the original superhydrophilicity of micro/nano-textured metal or metal oxide

surfaces. *Journal of Colloid and Interface Science*, *628*, 534–544. https://doi.org/10.1016/j.jcis.2022.08.039

Mason, L. (2007). Realistic Specific Power Expectations for Advanced Radioisotope Power Systems. *Journal of Propulsion and Power*, *23*(5), 1075–1079.

Mason, L., Poston, D., & Qualls, L. (2008). *System Concepts for Affordable Fission Surface Power*.

McCroskey, D. M., Abell, G. C., & Chidester, M. H. (2000). *Aeroglaze Z306 black paint for cryogenic telescope use: Outgassing and water vapor regain* (P. T. C. Chen & O. M. Uy, Eds.; pp. 119–128). https://doi.org/10.1117/12.400824

NASA TechPort. (2023). *Advanced Thermal Management Technologies to Enable Lunar and Martian Missions*. NASA Space Technology Misiion Directorate. https://techport.nasa.gov/strategy

Sovie, R. J. (1987, August 10). SP-100 Advanced Technology Program. *22nd Intersociety Energy Conversion Engineering Conference*. 22nd Intersociety Energy Conversion Engineering Conference, Philadelphia, Pennsylvania. https://doi.org/10.2514/6.1987-9232

Tarau, Calin & Maxwell, Taylor & Anderson, William & Wagner, Corey & Wrosch, Matt & Briggs, Maxwell. (2016). Status of the Development of Low Cost Radiator for Surface Fission Power - III. 10.2514/6.2016-4705.

Toffoli, A., Parisi, L., Bianchi, M. G., Lumetti, S., Bussolati, O., & Macaluso, G. M. (2020). Thermal treatment to increase titanium wettability induces selective proteins adsorption from blood serum thus affecting osteoblasts adhesion. *Materials Science and Engineering: C*, *107*, 110250. https://doi.org/10.1016/j.msec.2019.110250

594